Sustainable Cities and Society 131 (2025) 106666

Contents lists available at ScienceDirect

Sustainable Cities and Society

journal homepage: www.elsevier.com/locate/scs

Modelling temperature variations in Birmingham, UK at the neighbourhood scale: Using ADMS-Urban climate model

Jian Zhong [a,b,*], Yanzhi Lu [b], Jenny Stocker [c], Victoria Hamilton [c], Kate Johnson [c]

[a] Computational Science and Engineering Group, Centre for Advanced Simulation and Modelling, University of Greenwich, London SE10 9LS, UK
[b] School of Geography, Earth & Environmental Sciences, University of Birmingham, Edgbaston, Birmingham B15 2TT, UK
[c] Cambridge Environmental Research Consultants (CERC), Cambridge CB2 1SJ, UK

ARTICLE INFO

Keywords:
Urban heat island
Urban climate modelling
ADMS-Urban
Neighbourhood scale

ABSTRACT

Cities have higher peak temperatures compared to surrounding rural areas. The urban-rural near-surface air temperature difference is known as the urban heat island (UHI) intensity. As extreme heat exposure can lead to adverse health effects, information on UHI characteristics of cities is important for future urban climate planning strategies. This study applied the ADMS-Urban climate model to investigate the key processes driving temperature variations in Birmingham, UK, at the neighbourhood scale. This urban climate modelling was configured with a range of input datasets (such as meteorological data, land use data, building data, etc.) and model performance was evaluated against the temperature measurement datasets from UK Met Office and Weather Underground, and satellite datasets. The spatiotemporal variations of near-surface air temperature in Birmingham, UK were captured by this model. Spatiotemporal absolute temperature and temperature perturbations for different months at 50 m × 50 m resolution were generated. Monthly averaged temperature varies between 2 °C and 20 °C in Birmingham, UK. Urban heat island effect (reflected by the temperature perturbations with regard to upwind rural temperatures) in summer was much stronger (up to 2 °C) than that in other seasons and higher in the built-up areas compared to that in rural areas. Cooling island effects of water bodies and green spaces can bring a monthly temperature reduction of up to 4 °C in the summer season. This modelling study can be further applied to explore the impacts of local urban heat island mitigation strategies.

1. Introduction

Urban heat island (UHI) refers to the phenomenon of the temperature of urban built-up areas being higher than that of the surrounding suburban and rural areas. The average difference between the near-surface temperature in urban and surrounding areas, known as UHI intensity (UHII), was found to be 7.7 °C on a global scale by Clinton and Gong (2013). UHII shows increasing trends in urban areas where urbanity increases and built-up areas expand (He et al., 2007; Levermore et al., 2018). Due to the increased risk of high-temperature exposure, UHI is believed to cause multiple adverse effects on the health of urban residents, especially during summer and heat waves. This includes the rising morbidity and mortality from circulatory and respiratory diseases due to heat stress, indirect hazards caused by ozone formed under high-temperature conditions (Chaston et al., 2022; Piracha & Chaudhary, 2022; Tong et al., 2021), and the effects of high temperature on mental health, such as anxiety and depression (Mirzaei et al., 2020). UHI also causes a 12% increase in urban building energy demand at the global level due to cooling loads (Santamouris, 2020). UHII has been quantified using a variety of methods such as field measurements based on mobile sensors or urban climate networks (Barrao et al., 2022; Kousis et al., 2021) and land surface temperature (LST) retrieval using remote sensing data (Ahmad et al., 2024; Khalil & Kumar 2024). Using satellite thermal infrared data to assess UHI has the advantages of high efficiency and spatial coverage, but is limited by satellite revisit cycles, the impact of cloud cover, and the differences between LST and air temperature (Gao et al., 2006; Sun et al., 2020; Xu et al., 2022).

Because of the growing impacts of UHI on health, energy consumption, and the environment, accurately modelling and predicting the intensity and spatial distribution of UHI is essential for devising effective mitigation strategies. UHI modelling is based on UHI's formation mechanisms and the factors that influence its development, which includes: land cover properties, specifically, artificial surfaces with high thermal admittance and low albedo tend to absorb and store solar

* Corresponding author.
E-mail address: jian.zhong@greenwich.ac.uk (J. Zhong).

https://doi.org/10.1016/j.scs.2025.106666
Received 22 August 2024; Received in revised form 14 March 2025; Accepted 18 July 2025
Available online 19 July 2025

radiation, while surfaces with low evapotranspiration rates weaken the ability of water to dissipate heat (Phelan et al., 2015; Vujovic et al., 2021); meteorological conditions, like wind speed, cloud cover, and precipitation (Lokoshchenko & Alekseeva, 2023; Zheng et al., 2023); anthropogenic activities in urban areas, including anthropogenic heat emissions (e.g. air-conditioning heat rejection); and pollutant and greenhouse gas emissions generated by human activities (Luo et al., 2020; Qian et al., 2023).

Various models have been applied to predict the spatial distribution of temperature in urban areas. Numerical weather predictions (NWP) models such as the Weather, Research and Forecasting model (WRF) and the UK Met Office Unified Model (UM) include schemes that represent heat exchanges specific to urban areas; WRF includes a number of urban canopy modules (Jandaghian & Berardi, 2020) and the UM incorporates the 'Met Office Reading Urban Surface Exchange Scheme' (MORUSES) (Theethai Jacob et al., 2023). These mesoscale NWP models usually have a maximum resolution of 1 km, although some schemes are applied at sub-km scales. However, urban materials and land use vary at metres resolution, and urban climate variations are discernible at these scales. Urban microclimate models are used to simulate and predict these urban climate variations. For example, ENVI-met, based on Computational Fluid Dynamics (CFD), is one of the most widely used models (Jänicke et al., 2021). It has been applied to the evaluation of temperature perturbations caused by blue and green infrastructure (such as water bodies, street greening, grasslands, and green roofs) (Abdulateef & Al-Alwan, 2022; Cao et al., 2022; Liu et al., 2023) and cool materials (Faragallah & Ragheb, 2022; Haeri et al., 2023). This model has the disadvantages of large computational demand and long computational time (up to several days for a neighbourhood scale computational domain), so it is more suitable for prediction at the neighbourhood scale rather than the city scale (Maggiotto et al., 2014). Another commonly used model is the ADMS-Urban climate model developed by Cambridge Environmental Research Consultants (Hamilton et al., 2014). ADMS-Urban calculates local perturbations of temperature and humidity boundary layer profiles that result from spatial land use and urban morphological variations at tens of metres resolution; this neighbourhood-scale model also accounts for anthropogenic heat from sources. The model can be applied at the city scale but is also suitable for assessing the impact of localised land use changes on ambient temperatures (Hamilton et al., 2014) and energy use (Virk et al., 2015). Aktas et al. (2017) assessed the sensitivity of model outcomes to building material descriptors and Aktas et al. (2020) used model outputs as input to a range of thermal comfort calculations, specifically heat index, apparent and equivalent temperature. Biggart et al. (2021) implemented ADMS-Urban climate model to investigate the canopy layer urban heat island in Beijing. They found that modelled nocturnal UHI were more influenced by anthropogenic heat emissions in winter, compared with land surface radiative effects. Wang et al. (2019) applied ADMS-Urban climate model to simulate UHI in Kuala Lumpur, Malaysia. Their model clearly captured the spatial temperature variations as derived from satellite imagery. Maggiotto et al. (2014) compared the performance of ADMS-Urban climate model and ENVI-met model in temperature predictions in Lecce, Italy. They found that ADMS-Urban has more accurate temperature cycle prediction results than ENVI-met, especially at night. Tiwari et al. (2021) implemented ADMS-Urban climate model to examine the impact of changes in green infrastructure on the spatial distribution of urban temperature in Guildford, UK. They demonstrated that trees played the most important role in reducing UHI compared with green roof and grassland. However, current city-scale temperature modelling based on ADMS-Urban shows that there is still a gap between the modelled results and the actual air temperature distribution, and the distribution patterns of those gaps and their causes have not yet been sufficiently discussed. For example, while the simulation of ADMS-Urban is based on land cover-related parameters, it remains unclear whether the model exhibits differential accuracy across different land cover types.

Birmingham is a typical British industrial city. Since the industrial restructuring of the 1970s, this type of city has undergone extensive urban regeneration, resulting in land use change (Lee et al., 2016; Murie et al., 2005). Moreover, benefitting from a series of green and open space planning initiatives, such as the Green Living Spaces Plan and the Parks and Open Space Strategy, the quantity of green infrastructure in Birmingham is increasing (BCC, 2006, BCC, 2013). Due to these land cover changes, ADMS-Urban provides a valuable tool for simulating UHI in Birmingham. The study aimed to configure the ADMS-Urban climate model to simulate spatiotemporal variations of near-surface air temperature and urban heat island intensity in Birmingham, UK, at the neighbourhood scale, in order to evaluate the performance of the model in British industrial cities as represented by Birmingham. In addition to assessing the accuracy of the model in predicting temporal temperature changes, this article discusses whether the accuracy of the model's predictions varies across land use types. The results of the assessment will provide a foundation for the future application of the ADMS-Urban model in predicting UHI changes caused by land use changes in this type of industrial city.

This article is structured as follows: Section 2 describes the ADMS-Urban climate modelling approach, model configuration and input datasets. Section 3 presents the model evaluation and the results of temperature maps. Section 4 discusses the evaluation and results. Finally, Section 5 gives conclusions of the study.

2. Methods

2.1. ADMS-Urban climate model

ADMS-Urban upwind temperature and humidity boundary layer profiles are calculated hourly from surface meteorological measurements recorded outside the modelled urban area. Temperature and humidity variations within the domain are derived from perturbations to the surface sensible heat flux, ΔH, which are calculated from a perturbed version of the surface energy balance equation, specifically (Maggiotto et al., 2014):

$$\Delta H = \Delta Q^{*} - \Delta G - \Delta LH \quad (1)$$

where ΔQ^{*}, ΔG and ΔLH are the local short-wave net radiation, ground heat flux and latent heat flux perturbations, respectively. These three perturbation flux terms (Eq. (1)) are estimated from the spatial variation of land use and urban morphology within the urban area: ΔQ^{*} relates to albedo and building geometry; ΔG is derived from thermal surface properties; and ΔLH corresponds to the availability of surface moisture. The underlying coupled system of equations that govern heat and moisture processes and are solved within the model are described in Carruthers and Weng (1992) and Raupach et al. (1992). Temperature variations with altitude are accounted for, and the model additionally allows for the dispersion of the heat emitted from anthropogenic sources such as buildings and traffic, including the effects of the hourly variations of emission rates. Further details of the model formulation are given by Biggart et al. (2021).

The model takes hourly meteorological data as input, including upwind near-surface temperature and humidity values, cloud cover, wind speed and direction. The ADMS-Urban meteorological pre-processor converts these into parameters that describe the atmospheric boundary layer in terms of stability and allow the formulation of boundary layer profiles representing upwind conditions. A series of files that represent the in-domain spatial variation of surface albedo, surface resistance to evaporation, surface roughness, thermal admittance and building density are also required as input to the model. Terrain elevation data and anthropogenic heat emissions (road and/or volume sources) are optional inputs.

ADMS-Urban performs hourly calculations and outputs are hourly, for example time series corresponding to locations where temperature

measurements are being recorded, or period averages. The model calculates absolute values of temperature and humidity, and also perturbations to upwind values. For most studies, it is these perturbations that are analysed because they correspond to the urban heat island increment.

2.2. Meteorological datasets and model domain

In this study, meteorological data was sourced from both Met Office (via the Met Office Weather Observation Website) and Weather Underground (WU). Met Office data is considered to be reliable due to standard measurement procedures (Hahn et al., 2022). Despite being considered less reliable, WU data provides additional data points that are useful for evaluating model results. The study required meteorological measurements upwind or on the edge of the model domain, as input, in addition to sites within the model domain, for evaluation of model output.

All available meteorological sites from the Met Office in the vicinity of the model domain were considered for inclusion. Sites were selected based on the duration of data availability within the model year and their distance from the model domain. Five Met Office sites were used as inputs to the model: Elmdon (Birmingham airport), as a central site to prescribe prevailing wind; Coton-in-the-Elms (north upwind domain); Coleshill (east upwind domain); Alvechurch Weather (south upwind domain); and Stourbridge (west upwind domain). Three Met Office sites within the model domain were suitable for temperature evaluation: Coleshill, Elmdon and Winterbourne. There are 35 WU sites in the vicinity of the model domain. Since WU is not quality-assured like Met Office datasets (Lascano et al., 2024), they were not used as upwind domain sites. Only those WU sites located in the modelling area (the purple square obtained by symmetric expansion along the short side of the blue box in Fig. 1 whose side length is equal to the original long side of the blue box) were suitable to be applied as evaluation sites. Among those WU sites in the modelling area, sites with insufficient temporal coverage, i.e., lacking records for some months of 2019, were also excluded. After further removing the sites that are considered outliers (marked as grey points in Fig. 1), 10 out of the 35 WU sites were deemed suitable for inclusion as evaluation sites. Selected sites are summarised in Fig. 1.

The ADMS-Urban climate model requires upwind meteorological parameters, including temperature, relative humidity, cloud cover, and land use parameters, including surface roughness, albedo, surface resistance to evaporation and thermal admittance. For the land use parameters, a three-cell buffer region around the edge of the domain is assigned parameter values based on their respective upwind meteorological sites. To create the upwind dependent meteorological input file, wind speed and direction were primarily taken from the central Birmingham Elmdon site. For hours when this data was unavailable, data were taken from the nearby easterly Coleshill Met Office site. If this data was also missing, then data was taken from the Coleshill WU site. When wind direction indicated calm conditions, linear interpolation between available data points was performed. Low wind speeds were set to a minimum value of 0.3 $m.s^{-1}$ for input into the model. As the majority of upwind meteorological sites were missing cloud cover, these values were also obtained from the central site. If the central site lacked cloud cover data, Coleshill data was used.

Wind sectors were defined by the area contained within lines bisecting the radial directions between the centre of model domain and respective upwind sites. For each meteorological line, corresponding to each hour of the input file, the wind direction angle determined which upwind site to use for temperature and humidity parameter values. If upwind parameter values were unavailable, the average temperature and/or humidity from all of the upwind sites were used.

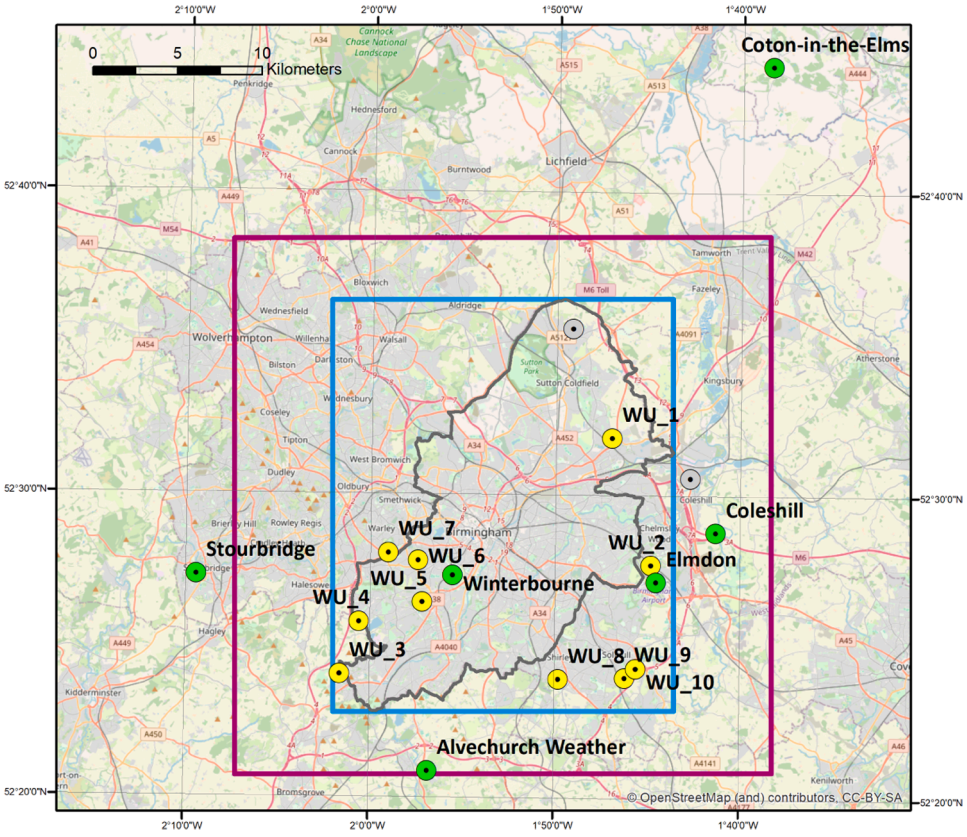

Fig. 1. Map of Birmingham and the surrounding areas showing model domain (blue box) upwind domain (purple box) surround Birmingham City (grey outline). Met office sites used in this study are shown as green dots, weather underground sites used in this study are shown as yellow dots.

2.3. Land cover datasets

Three land cover datasets were obtained to better represent the land cover for the area in this study. The first dataset was the 2019 land cover map published by the UK Centre for Ecology & Hydrology (UKCEH) (Morton et al., 2020), which is a raster dataset at 25 m × 25 m resolution. In areas other than urban and suburban, this dataset provides the most detailed land cover classification system at a high spatial resolution. Different kinds of grassland, woodland, and other natural land cover types are distinguished in this dataset. There are 21 land cover classes in this dataset, 13 of which are present in Birmingham and its surrounding area in this study. The second dataset was the vector map from OpenStreetMap (OpenStreetMap, 2019). The data from 2019 for the four counties covering the study area (West Midlands, Staffordshire, Worcestershire and Warwickshire) were obtained. OpenStreetMap provides detailed land use type information of urban and suburban areas, in particular the functions and attributes of buildings, which are not available in the UKCEH land cover map. The specific layers used from this dataset in this land cover mapping process were “buildings”, “land use”, “railway”, “water” and “pois (points of interest)”. The third dataset was Open Roads (obtained as a linear shapefile) from the Ordnance Survey (OS), downloaded via Digimap (Digimap, 2024). This dataset provides information on road classification, allowing for the creation of buffers for roads by class. These three land cover datasets were then combined to map the land use distribution for the study area, as shown in Fig. 2. The specific processing steps are described in the Supplementary Information (Section S1).

2.4. Surface parameters

Each polygon feature in the land cover map (Fig. 2) was assigned its own thermal admittance, surface resistance to evaporation, and albedo values according to the land cover type. Table 1 shows the corresponding parameters and their sources for each land cover type from UKCEH. Table 2 shows the parameters corresponding to each land cover type from OpenStreetMap and OS data. The parameters corresponding to the land cover types in this are all obtained from the literature (Aktas et al., 2017; Biggart et al., 2021). The classification of land use in Biggart et al. (2021) was used to simplify the land cover data from these two datasets into 16 categories due to the complexity of the original data. The function or types of some of the building polygon features in Birmingham city center (the area within Birmingham Ring Road and near Jewellery Quarter) were not recorded in OpenStreetMap. Based on the functional zone in which these unclassified buildings are located, these were assigned the parameters of land use type ’Commercial, Communal facilities’. In addition, areas not covered by any land use type were filled by the type of ’Other’.

A polygon-type fishnet with a width and length of 640 cells was created to cover the whole study area. Each cell in this fishnet was 50 m × 50 m. This fishnet and the land cover layer were intersected and the Calculate Geometry tool was used to calculate the area of each polygon feature within each cell. After exporting the attribute table of this intercepted layer, the value for each of the three parameters (albedo, surface resistance to evaporation, and thermal admittance) in each cell was calculated by using Eq. (2) based on area-weighted average (Biggart et al., 2021; Goodchild & Lam, 1980):

$$\overline{x} = \frac{\sum_{i=1}^{n} x_i S_i}{\mathrm{A}} \tag{2}$$

where $\overline{x}$ indicates the weighted average value of the parameter corresponding to the cell, x_i is the parameter value of one single polygon feature in the cell, S_i indicates the area of this polygon feature in square meters and A is the area of the cell (2500 m^2). This weighted average value (Eq. (2)) provides the parameter values assigned to a given cell. The cells in the upwind domain are exceptions as their albedo, surface resistance to evaporation, and thermal admittance values are not obtained by the above formula. Instead, these cells are assigned the three parameter values corresponding to the land cover type of the nearby upwind weather stations. Finally, the attribute table was exported, containing the cell ID, cell centre location, and three parameter values. From this, albedo, surface resistance to evaporation, and thermal admittance files were created with their respective parameter values (Fig. 3). The parameters corresponding to each meteorological site used for model evaluation (Fig. 1) are shown in Table S1 in the Supplementary Information.

The model also takes as input two files that reflect the spatial variation in building density, which are derived from 3D building datasets, and calculated at a horizontal spatial resolution of 250 m. The surface roughness, $z0$ (Eqs. (3) and (4)), is calculated using the following expression (Macdonald et al., 1998):

$$\frac{d}{H} = 1 + (\lambda_P - 1)\alpha^{-\lambda_P} \tag{3}$$

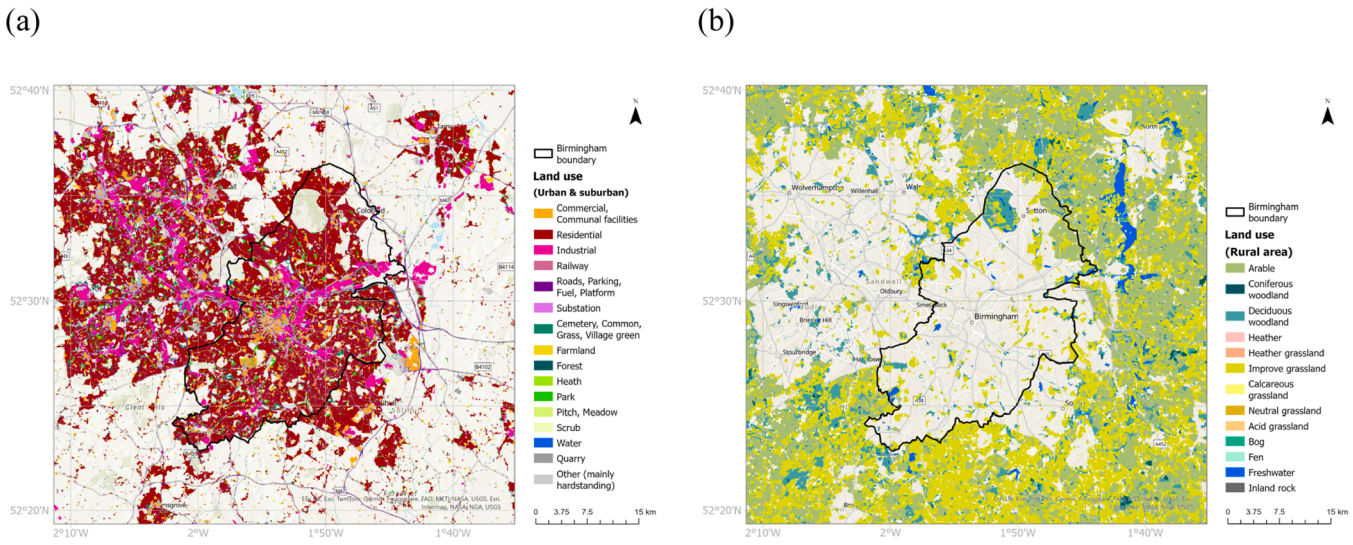

Fig. 2. Land cover of the study area, among which (a) is urban and suburban area whose land cover information is from OpenStreetMap and Ordnance Survey, (b) is rural area whose land cover information is from UKCEH.

Table 1
Albedo, surface resistance to evaporation and thermal admittance values assigned to each UKCEH land cover type.

UKCEH Land Cover Class	Land cover identifier	Albedo (-)		Surface resistance to evaporation (s m^{-1})		Thermal admittance (J m^{-2} $s^{-1/2}$ K^{-1})	
		Value	Reference	Value	Reference	Value	Reference
Deciduous woodland	1	0.16	Stull (1988)	115	Biggart et al. (2021)	1400*	Biggart et al. (2021)
Coniferous woodland	2	0.12	Stull (1988)	115	Biggart et al. (2021)	1400*	Biggart et al. (2021)
Arable	3	0.17	Biggart et al. (2021)	50	Oke (1987), Biggart et al. (2021)	1500*	Biggart et al. (2021)
Improve grassland	4	0.2	Biggart et al. (2021), Tiwari et al. (2021)	100	Tiwari et al. (2021)	600	Biggart et al. (2021), Tiwari et al. (2021)
Neutral grassland	5	0.2	Biggart et al. (2021), Tiwari et al. (2021)	100	Tiwari et al. (2021)	600	Biggart et al. (2021), Tiwari et al. (2021)
Acid grassland	7	0.2	Biggart et al. (2021), Tiwari et al. (2021)	100	Tiwari et al. (2021)	600	Biggart et al. (2021), Tiwari et al. (2021)
Fen	8	0.14	Hamilton et al. (2014)	100	Hamilton et al. (2014)	1420*	Hamilton et al. (2014)
Heather	9	0.2	Biggart et al. (2021), Tiwari et al. (2021)	100	Tiwari et al. (2021)	600	Biggart et al. (2021), Tiwari et al. (2021)
Heather grassland	10	0.2	Biggart et al. (2021), Tiwari et al. (2021)	100	Tiwari et al. (2021)	600	Biggart et al. (2021), Tiwari et al. (2021)
Inland rock	12	0.225	Biggart et al. (2021)	200	Biggart et al. (2021)	1850	Biggart et al. (2021)
Freshwater	14	0.08	Stull (1988)	10	Biggart et al. (2021)	1545	Oke (1987)

* Capped at 600 in this modelling study.

Table 2
Albedo, surface resistance to evaporation and thermal admittance values for each land cover type of OpenStreetMap and roads from OS (Aktas et al., 2017; Biggart et al., 2021).

Land cover type	Albedo (-)	Surface resistance to evaporation (s m^{-1})	Thermal admittance (J m^{-2} $s^{-1/2}$ K^{-1})
Cemetery, Common, Grass, Village green	0.2	70	600
Commercial, Communal facilities	0.12	200	1500
Farmland	0.17	50	1500*
Forest	0.16	115	1400*
Heath	0.2	100	600
Industrial	0.12	200	1750
Other (mainly hardstanding)	0.05	200	1205
Park	0.2	115	600
Pitch, Meadow	0.19	70	600
Quarry	0.08	200	2220
Railway	0.08	200	1150
Residential	0.18	150	1500
Roads, Parking, Fuel, Platform	0.08	200	1205
Scrub	0.17	70	600
Substation	0.08	200	1500
Water	0.08	10	1545

* Capped at 600 in this modelling study.

$$\frac{z_0}{H} = \left(1 - \frac{d}{H}\right) \exp\left\{ - \left[\frac{0.5 \beta C_D \lambda_F}{\kappa^2} \left(1 - \frac{d}{H}\right) \right]^{-0.5} \right\} \quad (4)$$

where d is the displacement height, H is the average building height, λ_P is the building plan area ratio, λ_F is the building frontal area ratio, von Karman constant $\kappa = 0.4$, the drag coefficient $C_D \sim 1$, and α and β are constants. The values of α and β are chosen to represent a staggered array of buildings, giving values of 4.43 and 1.0 respectively, following Di Sabatino et al. (2010). Note that here the influence of surface obstacles other than buildings are not accounted. For example, trees and wooded areas are neglected. However, this omission will most likely have only a small impact on modelled temperatures because surface wetness, albedo and thermal admittance dominate modelled temperature variations. The second building density parameter, the normalised building volume, NBV (Eq. (5)), is simply calculated as (Biggart et al., 2021):

$$NBV = H \lambda_P \quad (5)$$

In terms of terrain elevation data used in the modelling, a 250 m grid was extracted from the Ordnance Survey 'OS Terrain 50′ data product using a pointwise method.

2.5. Landsat satellite dataset

Remote sensing data, represented by Landsat, are widely used to retrieve land surface temperature (LST). Although the LST obtained from remote sensing data is different from the air temperature recorded by weather stations, there is a certain correlation, so LST from remote sensing data can also be used to validate the air temperature outputs of an urban climate model (Biggart et al., 2021; Wang et al., 2019). The correlation between LST and air temperature can be affected by factors such as season, climate, and topography (Naserikia et al., 2023; Peng et al., 2020). In our study area, Birmingham, previous research has shown that in summer, there is a strong correlation between LST and the air temperature at a neighbourhood scale (Azevedo et al., 2016). Although there are still some differences between the two temperatures at the city scale, in instances where there is limited coverage of urban weather stations, LST retrieval based on remote sensing data is a feasible method for the validation of the air temperature output of ADMS-Urban.

Landsat 8 was used as the remote sensing data source. It provides visible and near-infrared (NIR) data at 30 m resolution, and thermal infrared data at 100 m resolution (USGS, 2019). Landsat 8 data was obtained from the United States Geological Survey (USGS) Earth Explorer. The data used in this study was acquired at 10:58 AM UTC on 26 August 2019. Data from this day had the lowest cloud cover among available Landsat 8 data for our study area in the summer of 2019; land cloud cover of the tile was 4.14 %, and no clouds were visible in the study area, so cloud removal process was not needed. The Worldwide Reference System (WRS) path and row of the tile used are 202 and 24.

LST is retrieved by using QGIS Land Surface Temperature Plugin developed by Isaya Ndossi and Avdan (2016). Landsat 8 Thermal Infrared Sensor (TIRS) band, stored as digital numbers (DN), is converted to radiance and then to brightness temperature. Among the two TIRS bands (10 and 11) of Landsat 8, due to the calibration uncertainty in Band 11, we only use Band 10 to obtain the brightness temperature (Avdan & Jovanovska, 2016). Afterwards, the red (Band 4) and NIR (Band 5) bands were used to calculate normalised difference vegetation index (NDVI) and estimate land surface emissivity (LSE) by using the NDVI threshold LSE estimation algorithm (Isaya Ndossi & Avdan, 2016). Finally, we used the Plank Function to obtain LST (Eq. (6)) (Artis & Carnahan, 1982):

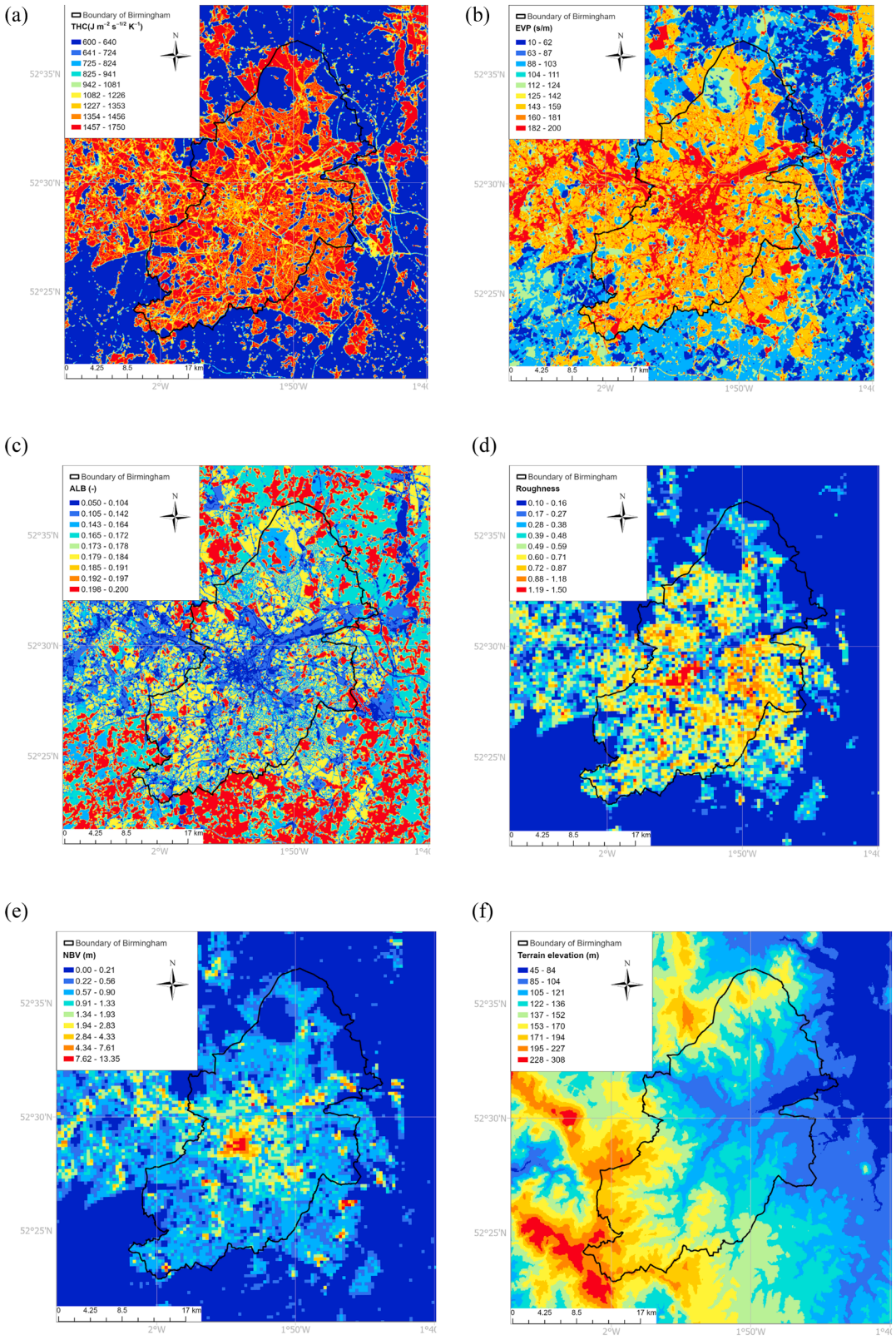

Fig. 3. Surface characteristics in the region of Birmingham at 50 m × 50 m resolution: (a) thermal admittance, (b) surface resistance to evaporation, (c) albedo, (d) surface roughness length, (e) normalised building volume and (f) terrain elevation.

$$T_s = \frac{BT}{\left\{1 + \left[\frac{\lambda \cdot BT}{\rho}\right] \cdot ln\varepsilon\right\}} \tag{6}$$

where T_s is LST (K), BT is brightness temperature (K), λ is the wavelength of emitted radiance (10.8 μm on Landsat 8 Band 10) (Sajib & Wang, 2020). ε is LSE. $\rho = 1.438 \times 10^{-2}$ mK (Isaya Ndossi & Avdan, 2016). This LST retrieval method has been applied and proven effective in previous peer-reviewed research articles (Neog, 2021; Nascimento

et al., 2022; Roy et al., 2021).

3. Results

The results of the evaluation of modelled temperature values against near-surface measurements are presented in Section 3.1. The spatial distribution of modelled temperatures is compared to satellite imagery in Section 3.2. These model evaluation results are followed by a presentation of modelled monthly average temperatures, both absolute, and the urban heat island intensity (UHII) (Section 3.3).

3.1. Model evaluation using surface measurements

For the near-surface measurement evaluation, the model was configured to generate hourly modelled temperature datasets at the receptor locations at the Met Office and Weather Underground measurement sites (Fig. 1). The ADMS-Urban climate model (Linux version) was executed on the University of Birmingham's BlueBEAR HPC using a single core. The annual simulation was split into six runs, each covering two months. The average elapsed time for a two-month run was about 44 h. Model evaluation was conducted by generating statistics and graphs that compared the modelled and observed hourly temperature datasets.

Fig. 4(a) and (b) show monthly variations of modelled and observed absolute temperatures, and temperature perturbation (UHII), respectively, averaged over all receptor locations. The observed monthly average temperatures range from approximately 4 to 18 °C over the year, and the corresponding UHIIs on average remain positive for the full year, in the range 0.1 to 0.4 °C. As the model uses upwind measurement as input, the absolute values of modelled temperature compare well with the observations. However, whilst the modelled UHII compares well with the observations in the summer months, there is relatively large under-prediction during the winter, spring and autumn. The most likely explanation for this under-prediction is the absence of anthropogenic heat sources in the modelling. Detailed UHI modelling by Bohnenstengel et al. (2014) using MORUSES showed that anthropogenic heat sources increase the UHII by 1 °C in May and 1.5 °C in December at a central London location. The current modelling of the West Midlands gives a winter under-prediction of approximately 0.6 °C (as an average over a range of measurement sites), which is broadly consistent with the conclusions from the London study. The remaining evaluation presented in this paper focuses on the summer months (June, July and August), where anthropogenic heat sources can be neglected.

In general, temporal variations in temperature resulting from changes in solar radiation are significantly larger in magnitude than spatial variations in temperature resulting from changes in land use type and material. Fig. 5(a) shows frequency scatter plots comparing hourly modelled and observed absolute temperatures, for all sites in the urban area for the summer months. The full range of temperatures varies between <10 °C to well over 30 °C, and model agreement is good; this outcome would be expected because the model uses upwind temperature measurements as input, which dominate model outputs in terms of diurnal variability. Fig. 5(b) shows a similar plot but comparing the upwind observed (i.e. rural) temperatures (which are the same for all sites) to the urban observed absolute temperatures. This comparison shows that there is relatively little difference between upwind rural and urban measurements, but we note that this study is attempting to replicate these perturbations to the upwind values, which represent the UHII. Inspecting the statistics corresponding to these plots, the modelled temperatures compare better to the urban observed values than the upwind values in terms of mean bias (−0.14 compared to −0.28). A robust highest concentration (RHC, shown as Eq. (7)) statistic (Perry et al., 2005), a measure of higher values within a dataset commonly used in evaluation of air pollution model outputs, can be expressed as (Cox & Tikvart, 1990):

$$RHC = T(n) + (T - T(n))\ln\left(\frac{3n-1}{2}\right) \tag{7}$$

where n is the number to represent the upper end of the distribution, taken to be 26; T is the average of the $n-1$ largest values; $T(n)$ is the n^{th} largest value. The observed, modelled and upwind values of $T(n)$ are 35.5 °C, 35.2 °C and 33.0 °C respectively, which indicates that the model appears to capture the magnitude of higher temperatures recorded in the urban area. In terms of a simpler metric, the maximum hourly temperature, the trend is similar, with the observed, modelled and upwind RHC values being 34.8 °C, 35.1 °C and 33.0 °C, respectively.

Fig. 6(a) shows diurnal variations of modelled and observed UHII averaged over all receptor locations. The model agrees well on average, and agreement is good on an hourly basis overnight. The model does not, however, capture the lower temperature perturbations in the early morning, and under-predicts the rate at which the UHII grows during the day, slightly missing the observed UHII peak at 19:00. Fig. 6(b) compares the modelled and observed UHII at one of the Met Office sites, Elmdon, where the average summer UHII is over 1 °C in the late evening. Here, the model better captures the hourly variation, although there is still a tendency for over-prediction in the early morning. Figs. 6(c) and (d) present the same comparisons for two of the Weather Underground (WU) sites. The first, which is a WU personal weather station at Harborne with station ID IENGLAND381, shows a general model over-prediction, particularly in the early morning. There is better agreement at the second site (IMINWORT2), which records a relatively high UHII of over 2 °C in the late evening. In terms of the site parameters (Table S1), the thermal admittance, surface resistance to evaporation and albedo values are the same at both sites. Inspection of the areas using satellite imagery, we see that both sites are residential housing with gardens. However, the IENGLAND381 site has significantly more

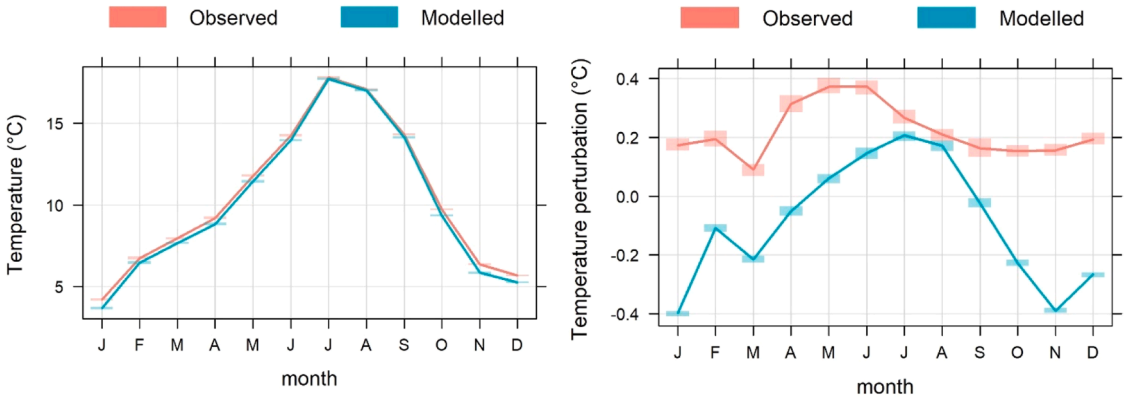

Fig. 4. Monthly variations of modelled and observed (a) absolute temperatures and (b) temperature perturbation (UHII) averaged over all receptor locations.

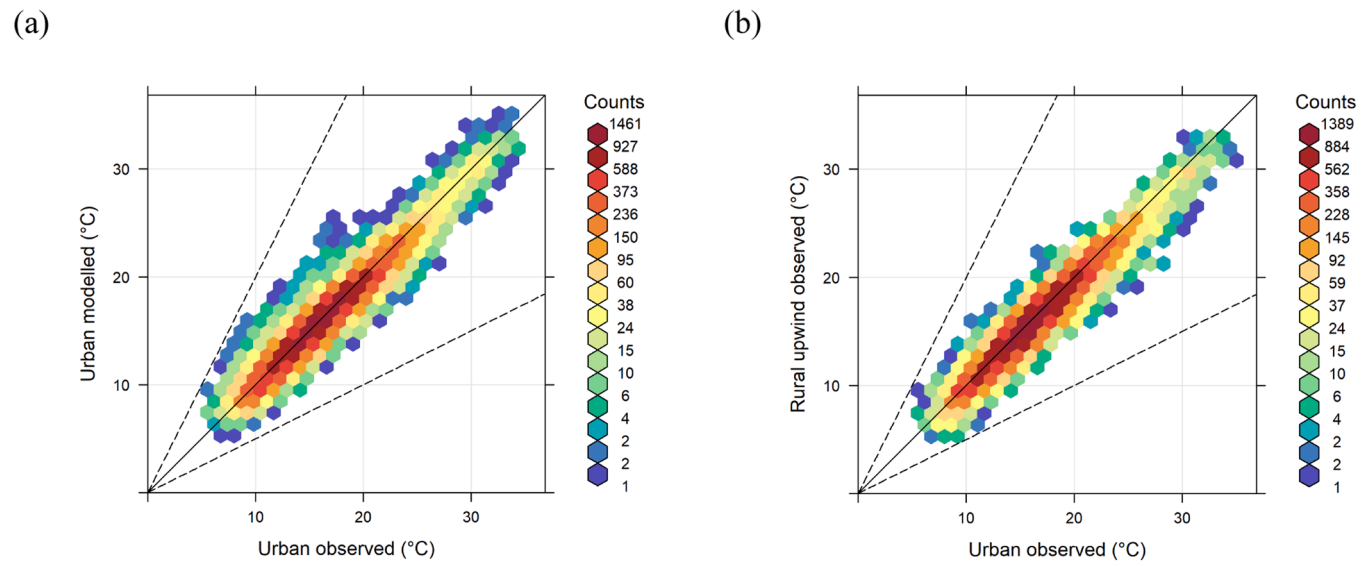

Fig. 5. Frequency scatter plots (a) between modelled and urban observed absolute temperatures, and (b) between rural upwind observed and urban observed absolute temperatures for all sites for the summer months (June, July and August).

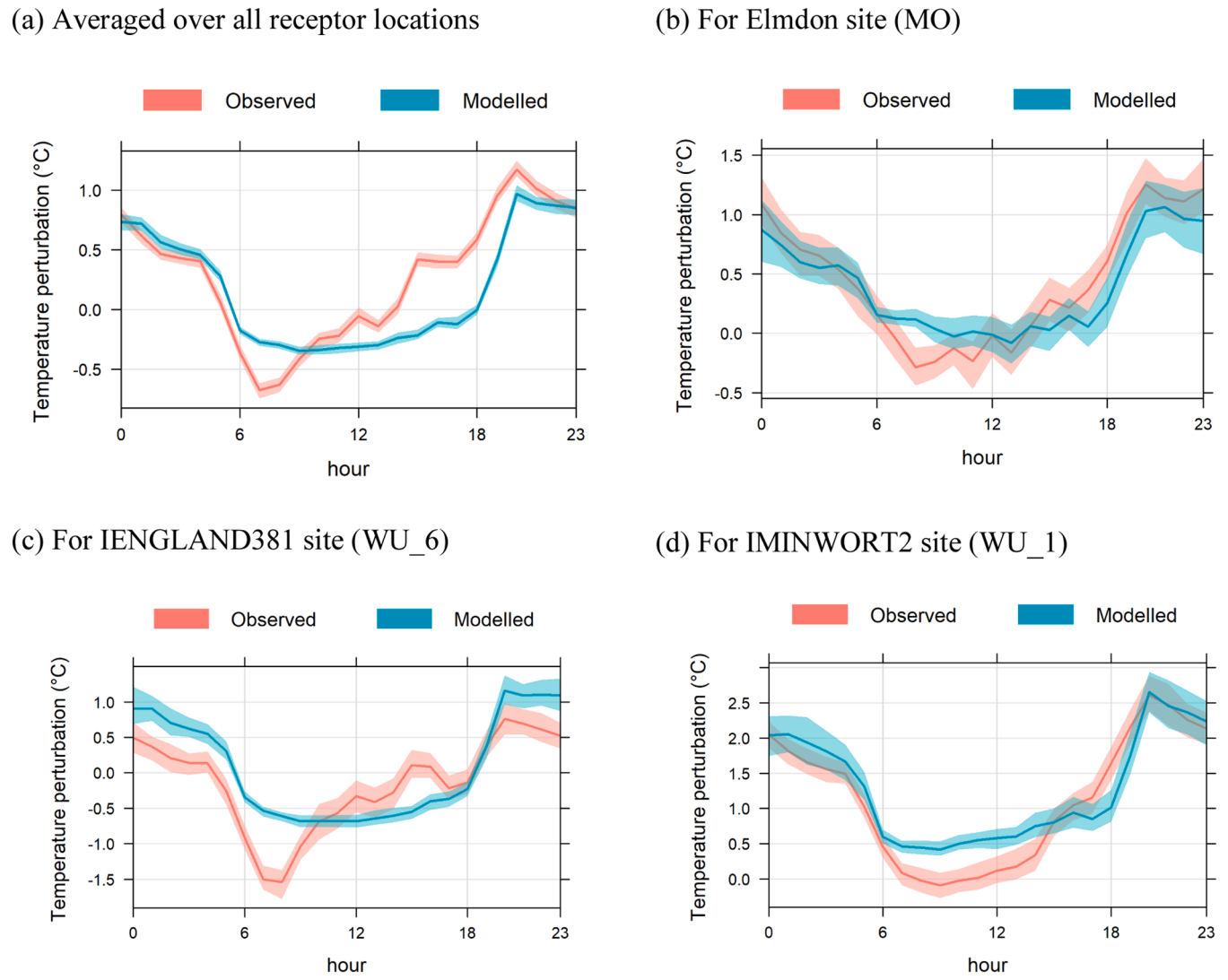

Fig. 6. Diurnal variations of modelled and observed temperature perturbation (UHII) averaged over all receptor locations, and for selected sites, respectively, for the summer months (June, July and August).

garden and tree coverage compared to houses and roads; and also IMINWORT2 is adjacent to a superstore and large car park. It is likely that these built structures lead to the relatively high UHII at IMINWORT2 compared to IENGLAND381. Recall that for the current study, the calculations of site parameters are a result of generic land use types e.g. 'residential' and therefore do not differentiate between the amount of greenery.

Fig. 7 shows the box and whisker plot of modelled and observed temperature perturbation (UHII) at all receptor locations for the summer months. The modelled and observed median values agree for most sites. In general, the ranges of modelled temperature are not as large as the observed on a site-by-site basis, in terms of both the inter-quartile and full range, which is expected as the model formulation and inputs correspond to average conditions; observed climate parameters would be expected to fluctuate more. Fig. 8 shows a scatter plot of average modelled and observed temperature perturbation (UHII) at all receptor locations for the summer months, corresponding to the median showed in Fig. 7. This shows the full range of average UHII, and good agreement at several sites, including all Met Office sites. It is worth noting that the UHII at the Met Office sites are small on average, because these are generally located away from very built-up areas. The model on average under-predicts the average UHII for WU sites, but generally replicates the diurnal patterns (Fig. 6). The under-prediction may again relate to the use of 'average' land use for all residential areas.

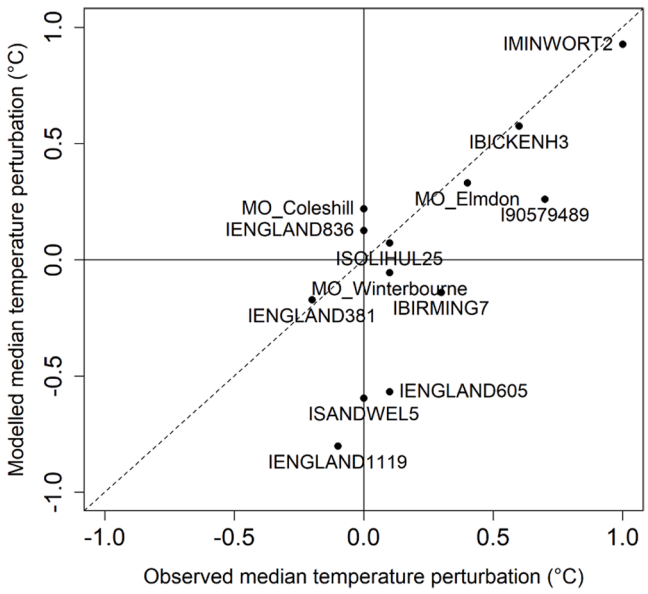

Fig. 8. Scatter plot between modelled and observed median temperature perturbations (UHII) for the summer months (June, July and August).

3.2. Model evaluation using satellite imagery

Fig. 9 shows modelled spatiotemporal temperature variation patterns compared with the Landsat 8 satellite image. Although modelled air temperature has lower values and smaller ranges than LST, the two temperatures show roughly the same spatial distribution pattern in Birmingham and its surrounding areas. It can be seen in the figure that, in general, both the modelled air temperature and LST in this area show a decreasing trend from the city centre outwards, with both high modelled air temperature (>23 °C) and LST (>30 °C) concentrated in Birmingham city centre, Bromford industrial area, Hams Hall, and the area near Birmingham airport, but also scattered in the suburban area of Birmingham. The areas with the lowest modelled air temperature are waterbodies (such as Kingsbury Water Park in the northeast of Birmingham) and the area in the southwest of the city (Clent Hills) (about 21 °C), which also have low LST values (about 23 °C). On the other hand, in Fig. 9b, areas with similar levels of LST to Kingsbury Water Park and Romsley are widely distributed, surrounding the urban area of Birmingham, including Sutton Park in the north of the city, but the model did not simulate low air-temperature values in most of these areas. This is the most significant difference in the spatial distribution of modelled air temperature and LST.

Fig. 10 shows the frequency of 50 m resolution modelled near-surface air temperatures and Landsat 8-derived LST (regridding the original 30 m resolution to the 50 m resolution used in the model for the purpose of comparison). In general, modelled air temperature and LST are positively correlated. The correlation between these two types of temperatures is more pronounced in areas where LST is close to or above 30 °C (i.e., urban areas, according to Fig. 9) and below 25 °C. In these areas, locations with higher LST generally correspond to higher modelled air temperatures. However, in areas with an LST of around 25 °C, the modelled air temperatures mostly range between 21.5 °C and

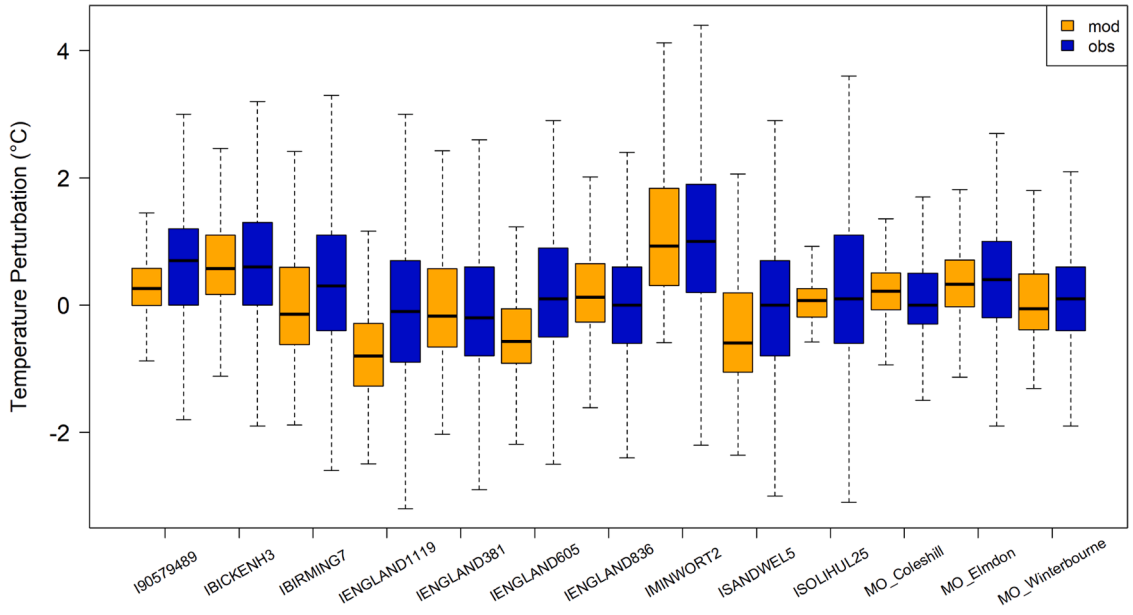

Fig. 7. Box plot of modelled and observed temperature perturbation (UHII) at all receptor locations for the summer months (June, July and August).

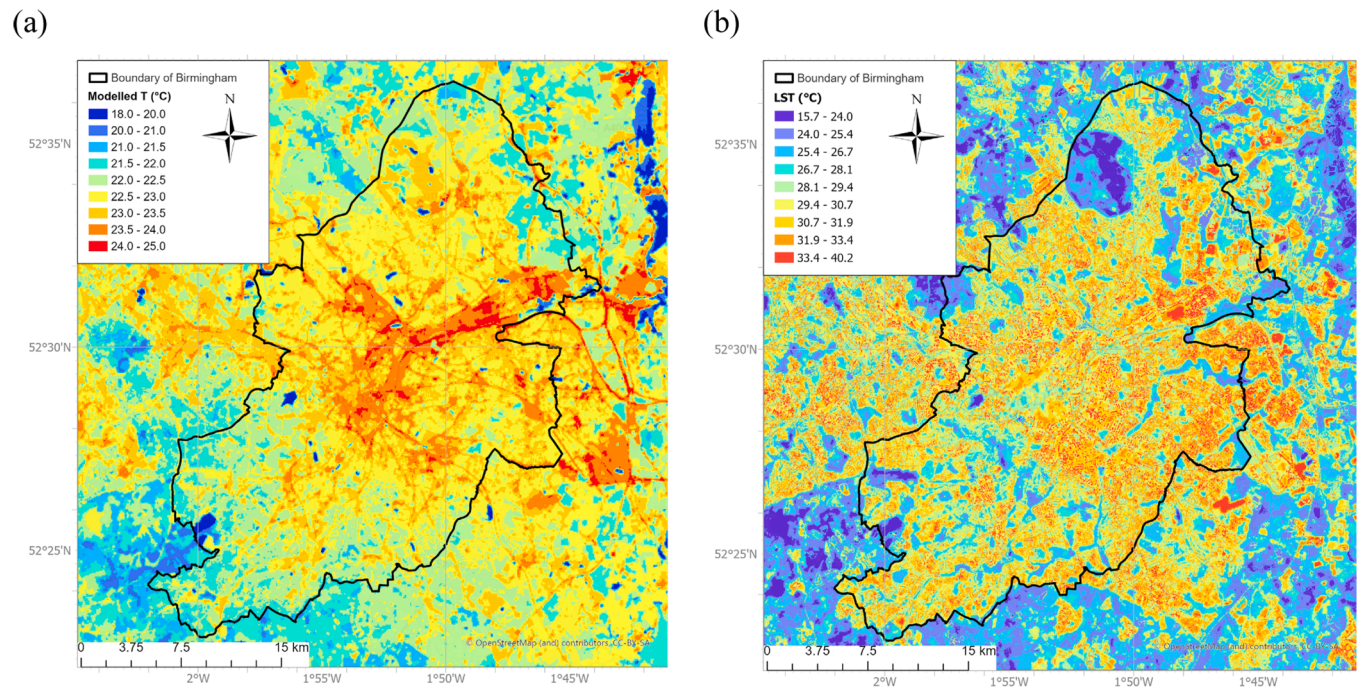

Fig. 9. (a) Modelled near-surface air temperature mapping at 50 m × 50 m resolution in Birmingham, UK and (b) Landsat 8 derived land surface temperature at 11 am GMT 26th August 2019.

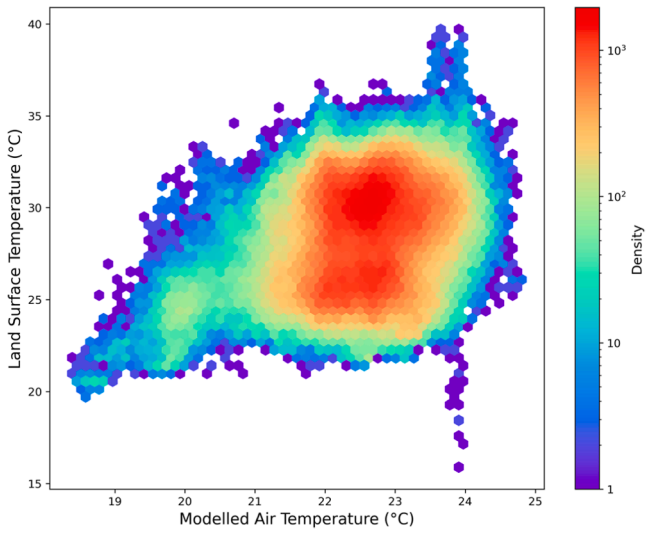

Fig. 10. Frequency of 50 m resolution modelled near-surface air temperatures and Landsat 8-derived land surface temperatures for 11 am GMT 26th August 2019.

23.5 °C, only slightly lower than those in areas where LST is close to or above 30 °C. This suggests that the model may overestimate air temperatures in regions with an LST of around 25 °C.

There are a total of 17 combinations of the three land-cover-related parameters (thermal admittance, surface resistance to evaporation, and albedo). Fig. 11 shows the relationship between modelled air temperature and LST for land cover types with different parameters. The land-cover-related parameters, modelled air temperature, and LST values used in this part of the result are from the centre point of each pixel in the 50 m × 50 m resolution modelling output dataset. Combined with Table 1 and Table 2, it can be found that the areas with LST of about 25 °C mainly belong to acid grassland, heath (heather) and improved grassland (thermal admittance = 600, surface resistance to evaporation = 100, and albedo = 0.2; number of points: 73,376 out of 409,600), followed by deciduous woodland (forest) (thermal admittance = 1400, surface resistance to evaporation = 115, and albedo = 0.16; number of points: 25,072 out of 409,600). Compared with other land cover types, their plots are located further to the lower right in scatter plot figures. In addition, we found that in some land cover types represented by farmland (thermal admittance = 1500, surface resistance to evaporation = 50, and albedo = 0.17; number of points: 42,204 out of 409,600), modelled T is concentrated in a small interval, while the actual LST varies greatly. The model does not capture the actual temperature differentiation in these areas.

3.3. Modelled monthly temperature maps

Fig. 12 shows modelled monthly average temperature for (a) January 2019, (b) April 2019, (c) July 2019 and (d) October 2019 at 50 m × 50 m resolution in Birmingham, UK. It is expected that monthly average temperature in January (winter season) is relatively lower than other months. Monthly average temperature ranges between 2 °C and 20 °C, with gradual increases in April (spring season) and July (summer season), followed by a decrease in October (autumn season). The trend in monthly average temperature was also reflected in Fig. 4. The relative lower temperature in southwest Birmingham is mostly caused by higher elevation. Monthly average temperature is relatively higher in urban areas than in rural areas. Relative lower temperatures are found in green areas and water bodies.

Fig. 13 presents the corresponding modelled spatiotemporal temperature perturbations (with regard to upwind rural temperatures) for (a) January 2019, (b) April 2019, (c) July 2019 and (d) October 2019 at 50 m × 50 m resolution in Birmingham, UK. Monthly average temperature in urban areas can be up to 2 °C greater than the upwind rural temperature in July. A stronger urban heat island effect (reflected by larger temperature perturbations) is found in the summer season due to the strong incident solar radiation. Cooling island effects of water bodies and green spaces can bring a monthly temperature reduction of 4 °C in the summer season.

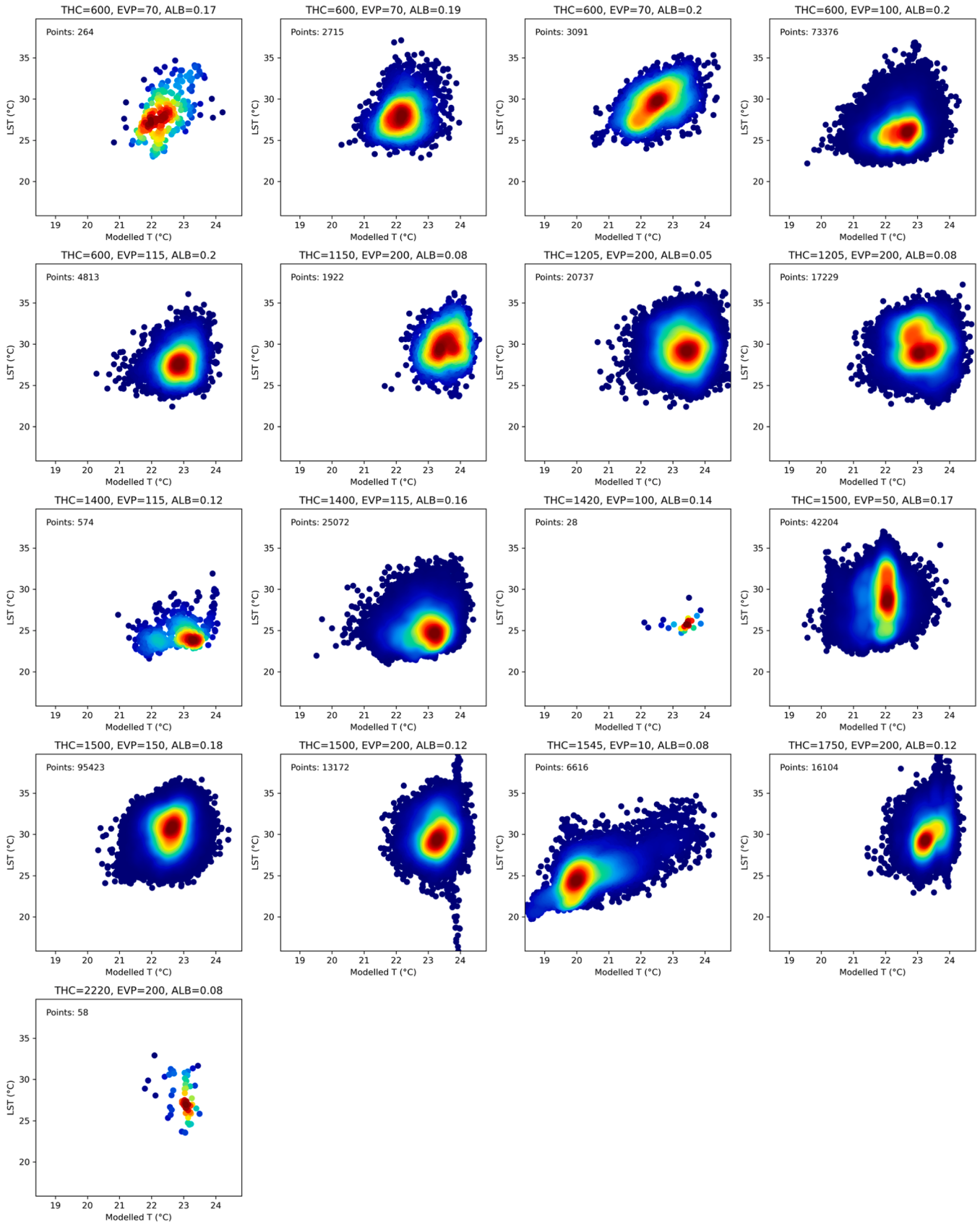

Fig. 11. Density scatter plots showing the relationship between LST and modelled T in the land cover types with each combination of the three parameters (thermal admittance, surface resistance to evaporation, and albedo).

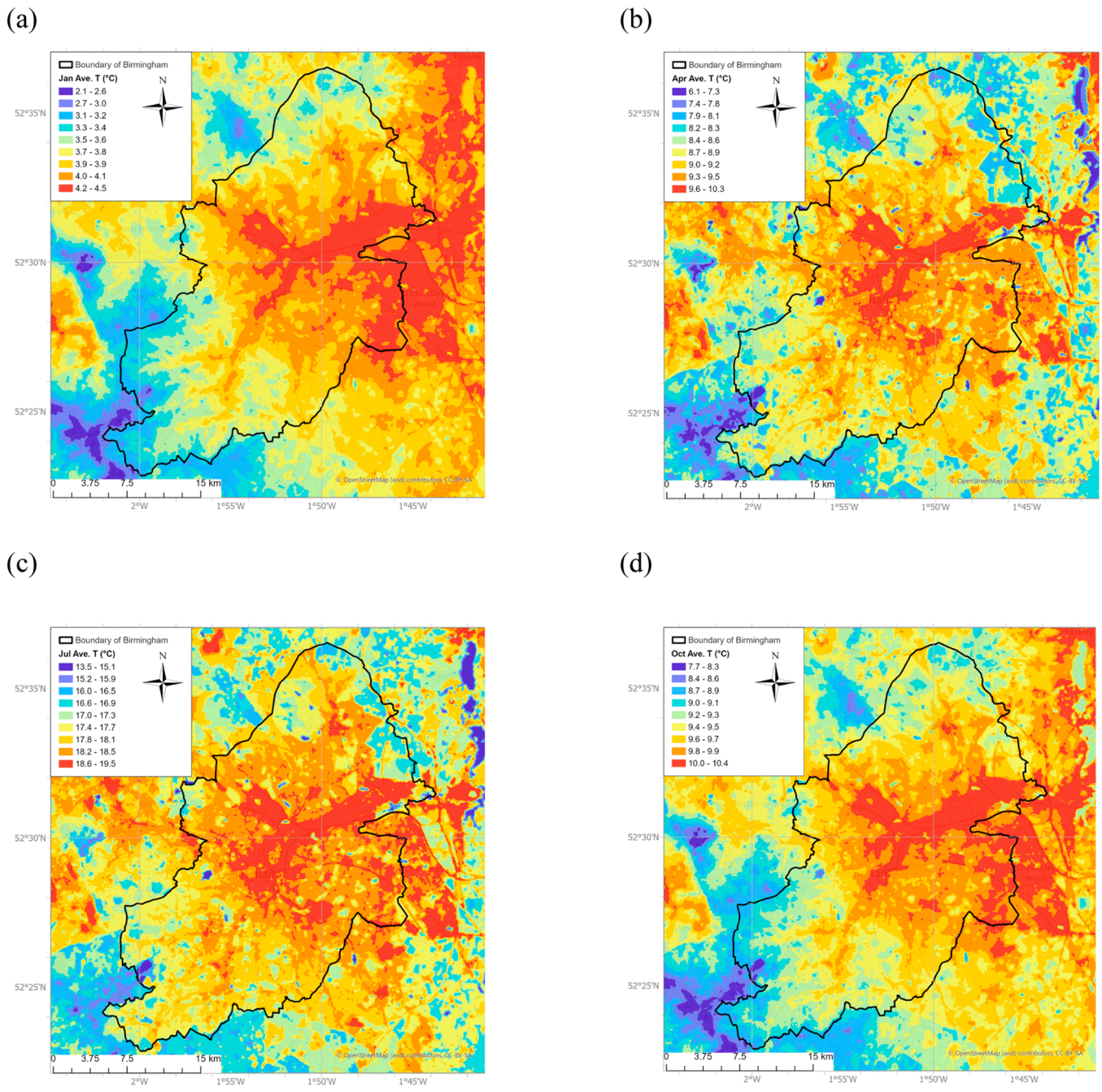

Fig. 12. Modelled monthly average temperature for (a) January 2019, (b) April 2019, (c) July 2019 and (d) October 2019 at 50 m × 50 m resolution in Birmingham, UK.

4. Discussion

Hourly air temperature results output by the model were compared with the air temperature measured by urban meteorological stations. This modelling study demonstrates both temporal (hourly, seasonal) and spatial variations in UHII in the Birmingham City area. Anthropogenic emissions sources have not been modelled (similarly to Wang et al. (2019)), which contributes to the model under-predictions in the winter, spring and autumn. Biggart et al. (2021) demonstrated that UHII in winter is dominated by anthropogenic heat emissions, which may be uncertain and underestimated by the model in their study for Beijing. The evaluation, therefore, focused on model performance during the summer months of June, July and August. As the model uses input temperatures from measurement equipment located upwind of the model domain, model predictions of absolute temperatures compare very well with measurements. Statistical analyses showed that the model has some skill in terms of predicting peak, absolute temperatures. The model broadly replicates the diurnal variations of temperatures at the majority of sites considered, although with some over-prediction in the early morning at some sites. The spatial variation in temperatures recorded on a site-by-site basis is generally well represented by the model, with three exceptions where the model under-predicts. The majority of the Weather Underground sites are located in residential areas, but the model inputs do not differentiate in terms of land usage, which is the likely explanation for the lack of agreement between model and observed temperatures at some sites. The low early morning temperatures not replicated by the model could also be associated with poor representation of the heat fluxes around dusk (Biggart et al., 2021).

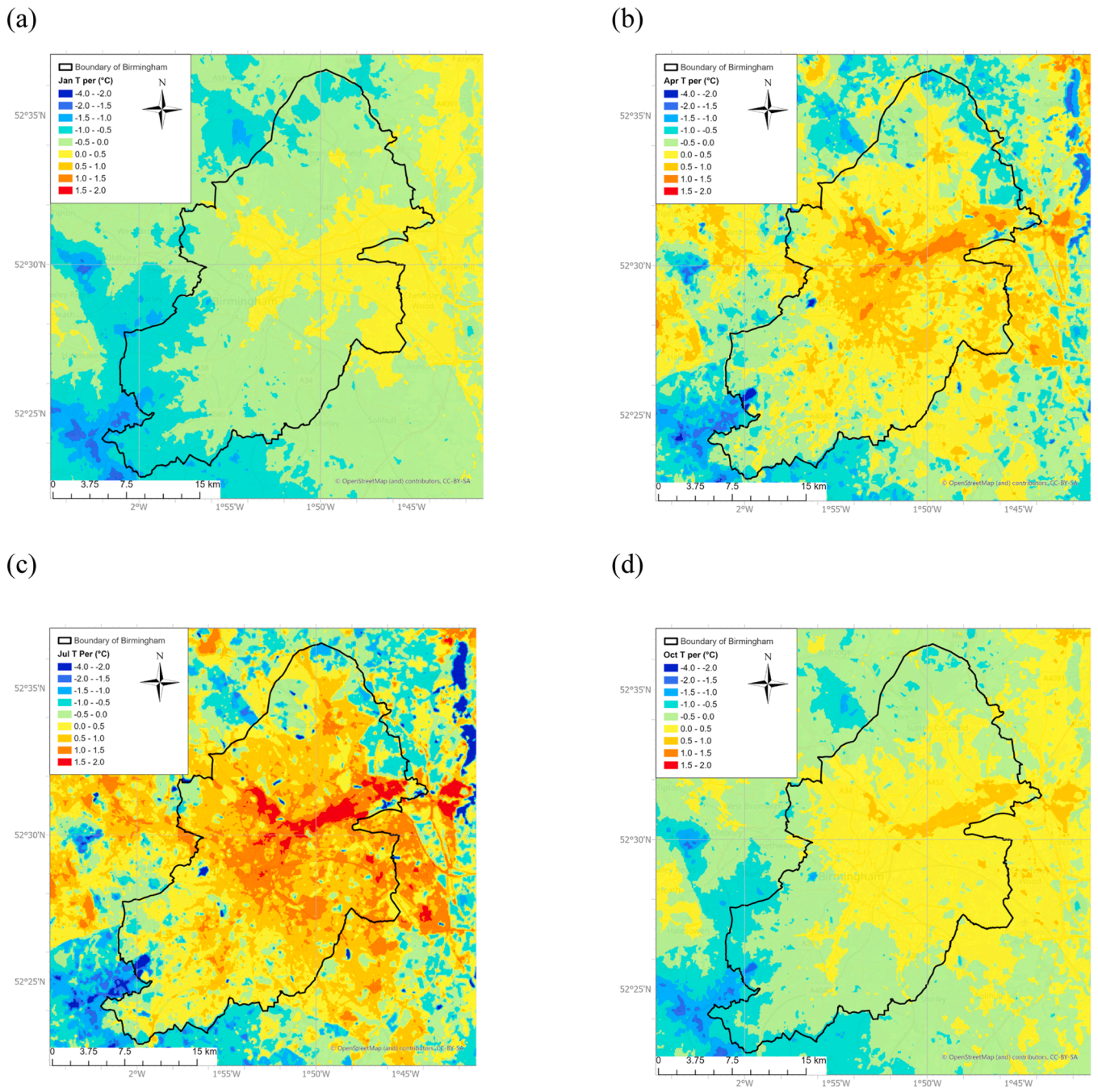

Fig. 13. Modelled monthly average temperature perturbation (UHII) for (a) January 2019, (b) April 2019, (c) July 2019 and (d) October 2019 at 50 m × 50 m resolution in Birmingham, UK.

LST derived from Landsat was applied in comparison with modelled air temperatures to evaluate model performance, according to its similarity to near-surface air temperatures (Xiang et al., 2023). The range of LST (11−45 °C) is much larger than that of modelled air temperature (18−25 °C), which is due to the difference in heating mechanisms between the surface and near-surface air (Phelan et al., 2015). Nevertheless, the performance of the model has been validated, according to the consistency of spatial distribution of LST and modelled air temperature shown in Fig. 9, as well as the correlation between these two types of temperature shown in Fig. 10. The model performs well in predicting the air temperature of some cold islands (for example, water bodies represented by Kingsbury Water Park and high-altitude areas like Clent Hills) and heat islands (mainly Birmingham city centre and industrial areas in Birmingham), which shows similar spatial distribution patterns with LST. However, compared with the air temperature-LST correlation result of another field research in Birmingham (Azevedo et al., 2016), the correlation between ADMS-Urban modelled air temperature and LST is relatively low, which means that the model may not adequately predict the temperature in some areas. Figs. 9, 10 and 11 show that compared with the distribution of LST, the model underestimates the air temperature difference between the city centre and the suburban/rural areas (LST is approximately 25 °C). In previously published papers, it has also been observed that the modelled T on the LST-Modelled T scatter plots shift toward the low values of LST (Biggart et al., 2021; Wang et al., 2019), which means this may be a common phenomenon in simulations based on ADMS-Urban. Although Biggart et al. (2021) suggested that increased humidity may be the reason for the unobvious temperature differentiation between urban areas and suburbs, our analysis of various

land cover types shows that the model might overestimate the temperature in some types of land cover, such as grassland, heather, and deciduous woodland (forest). Therefore, in future simulations using ADMS-Urban, the parameters corresponding to the above land cover types should be appropriately adjusted to correct the model performance. For example, we can increase the thermal admittance, decrease the surface resistance to evaporation, or increase the albedo (Oke, 1987; Stull, 1988).

The model's performance on farmland can be explained by the complexity of farmland. In this study, as well as previous studies (Biggart et al., 2021; Wang et al., 2019), farmlands were assigned unified parameters (albedo, surface resistance to evaporation, and thermal admittance). However, in reality, different types of farmlands may have different parameters due to the variety of crop species and irrigation conditions (Lei et al., 2024; Oke, 1987; Russell, 1980). In addition, in the UK, August is the beginning of the harvest season for some crops, such as wheat (Atkinson et al., 2005). The differences in the actual parameters corresponding to harvested and unharvested farmland may also affect the modelling results. Therefore, in future studies, parameters corresponding to some land cover types should be adjusted. In particular, farmland needs to be subdivided according to crop type and assigned different parameters to restore the actual albedo, surface resistance to evaporation and thermal admittance distribution to the greatest extent.

Monthly average temperature maps at 50 m × 50 m resolution in Birmingham, UK, can provide a unique and neighbourhood-scale temperature dataset, which captures urban materials and land use variation at the neighbourhood scale. Neighbourhood scale temperature maps could benefit the Climate Risk and Vulnerability Assessment (CRVA) mapping (Greenham, 2023). The openly available km scale monthly temperature map from Met Office's mesoscale NWP model was adopted in the current CRVA mapping at a variety of spatial resolutions for Birmingham (Greenham, 2023). Monthly averaged temperature varies between 2 °C and 20 °C, which reflects the seasonal variability of solar radiation. It is the highest temperatures in summer season and the lowest temperatures in winter season, which are most relevant to heat-related health risk assessment during extreme weather events (Biggart et al., 2021). Spatial variation of monthly averaged temperature is mainly induced by surface characteristics, as indicated in Fig. 3. Monthly average temperature perturbations (with regard to upwind rural temperatures) range between −4 °C and 2 °C. Higher temperatures in urban areas are mainly due to the higher thermal admittance (which absorbs more heat during the day and releases more heat during the night), and higher resistance to evaporation (highly urbanised areas with less green space and water bodies). Cooling island effects are also found for green spaces and water bodies, which is mainly due to the low resistance to evaporation, which was also identified by Wang et al. (2019) and Biggart et al. (2021). This also indicates that increasing green spaces, especially in cities, can be an effective mitigation measure for urban heat island (Tiwari et al., 2021).

Future research would be 1) to investigate anthropogenic heat emissions on temperature variations, 2) to examine the impact of Net Zero neighbourhood (housing retrofitting) on the mitigation of temperature, 3) to explore the impacts of tree planning scenarios on the mitigation of temperature, 4) to conduct heat-related health risk assessment of the mitigation scenarios using Climate-LAT tool (an extension of AQ-LAT tool, Hall et al. (2024)), and 5) to compare the neighbourhood temperature maps and 1 km regional scale temperature maps for the CRVA mapping (Greenham, 2023).

5. Conclusions

The ADMS-Urban climate model was configured and implemented to investigate spatiotemporal variations of near-surface air temperature and temperature perturbations in Birmingham, UK, at the neighbourhood scale. We demonstrated that ADMS-Urban is an effective tool for predicting UHI's temporal and spatial differentiation in a post-industrial city represented by Birmingham. On the temporal dimension, model evaluation showed that the ADMS-Urban climate model generally performed well to capture both absolute temperature and temperature perturbations. Modelled air temperature is generally positively correlated with LST derived from Landsat, and the two types of temperatures have similar spatial distribution patterns. The model is particularly successful in capturing urban heat islands in city centres and industrial areas, as well as cold islands, for example, water bodies. This suggests the potential for the ADMS-Urban model to be applied to future studies on UHI change in cities similar to Birmingham that are undergoing deindustrialisation and land use change. However, certain adjustments to the parameters corresponding to some land cover types are still needed to simulate the temperatures of these areas more accurately. We also quantified the UHII in Birmingham based on this modelling methodology. Spatiotemporal absolute temperature and temperature perturbations for different months at 50 m × 50 m resolution were generated. Monthly average temperature varies between 2 °C and 20 °C in Birmingham, UK. Urban heat island effect (reflected by the temperature perturbations with regard to upwind rural temperatures) in summer was much stronger (up to 2 °C) than in other seasons and higher in the built-up areas compared to rural areas. Cooling island effects of water bodies and green spaces can bring a monthly temperature reduction of up to 4 °C in the summer season.

Data availability

Met Office MIDAS meteorological data are available in Centre for Environmental Data Analysis, http://catalogue.ceda.ac.uk/uuid/dbd451271eb04662beade68da43546e1. The building data are available in https://digimap.edina.ac.uk. Temperature datasets at Weather Underground stations need to be requested from IBM.

CRediT authorship contribution statement

Jian Zhong: Software, Conceptualization, Writing – original draft, Funding acquisition, Visualization, Formal analysis, Methodology. **Yanzhi Lu:** Methodology, Visualization, Software, Writing – original draft, Formal analysis. **Jenny Stocker:** Funding acquisition, Software, Methodology, Writing – original draft. **Victoria Hamilton:** Methodology, Writing – review & editing, Software. **Kate Johnson:** Software, Writing – review & editing, Methodology.

Declaration of competing interest

The authors declare that they have no known competing financial interests or personal relationships that could have appeared to influence the work reported in this paper.

Acknowledgments

The authors acknowledge the University of Birmingham's BlueBEAR HPC service (http://www.bear.bham.ac.uk) for providing the computational resource. The authors also appreciate IBM for the provision of temperature datasets measured at Weather Underground stations.

Funding

This work has been supported by the UK's Research England SUPMO project (via the University of Birmingham's Institutional QR Policy Support Fund, Ref: PSF-24), NERC WM-Adapt project (Ref: UKRI/NE/B000279/1) and the University of Greenwich's "Multi-scale, Multi-disciplinary, Modelling for Impact" programme ($M^3$4Impact) which is funded by the Expanding Excellence in England (E3) fund of Research England (2024).

Supplementary materials

Supplementary material associated with this article can be found, in

the online version, at doi:10.1016/j.scs.2025.106666.

Data availability

Data will be made available on request.

References

Abdulateef, M. F., & Al-Alwan, H. A. (2022). The effectiveness of urban green infrastructure in reducing surface urban heat island. *Ain Shams Engineering Journal, 13*, Article 101526.

Ahmad, B., Najar, M. B., & Ahmad, S. (2024). Analysis of LST, NDVI, and UHI patterns for urban climate using Landsat-9 satellite data in Delhi. *Journal of Atmospheric and Solar-Terrestrial Physics, 265*, Article 106359.

Aktas, Y. D., Stocker, J., Carruthers, D., & Hunt, J. (2017). A sensitivity study relating to neighbourhood-scale fast local urban climate modelling within the built environment. *Procedia Engineering, 198*, 589–599.

Aktas, Y. D., Wang, K., Zhou, Y., Othman, M., Stocker, J., Jackson, M., Hood, C., Carruthers, D., Latif, M. T., D'ayala, D., & Hunt, J. (2020). Outdoor thermal comfort and building energy use potential in different land-use areas in tropical cities: Case of Kuala Lumpur. *Atmosphere, 11*, 652.

Artis, D. A., & Carnahan, W. H. (1982). Survey of emissivity variability in thermography of urban areas. *Remote Sensing of Environment, 12*, 313–329.

Atkinson, M., Kettlewell, P., Hollins, P., Stephenson, D., & Hardwick, N. (2005). Summer climate mediates UK wheat quality response to winter North Atlantic Oscillation. *Agricultural and Forest Meteorology, 130*, 27–37.

Avdan, U., & Jovanovska, G. (2016). Algorithm for automated mapping of land surface temperature using LANDSAT 8 satellite data. *Journal of Sensors*, Article 1480307, 2016.

Azevedo, J. A., Chapman, L., & Muller, C. L. (2016). Quantifying the daytime and night-time urban heat island in Birmingham, UK: A comparison of satellite derived land surface temperature and high resolution air temperature observations. *Remote Sensing, 8*, 153.

Barrao, S., Serrano-Notivoli, R., Cuadrat, J. M., Tejedor, E., & Sánchez, M. A. S. (2022). Characterization of the UHI in Zaragoza (Spain) using a quality-controlled hourly sensor-based urban climate network. *Urban Climate, 44*, Article 101207.

BCC, 2006. The Future of Birmingham's Parks and Open Spaces: Supplementary Planning Document, https://www.birmingham.gov.uk/downloads/file/1061/the_future_of_birminghams_parks_and_open_spaces_supplementary_planning_document.

BCC, 2013. Green Living Spaces Plan, https://www.birmingham.gov.uk/greenlivingspaces.

Biggart, M., Stocker, J., Doherty, R. M., Wild, O., Carruthers, D., Grimmond, S., Han, Y., Fu, P., & Kotthaus, S. (2021). Modelling spatiotemporal variations of the canopy layer urban heat island in Beijing at the neighbourhood scale. *Atmos. Chem. Phys., 21*, 13687–13711.

Bohnenstengel, S. I., Hamilton, I., Davies, M., & Belcher, S. E. (2014). Impact of anthropogenic heat emissions on London's temperatures. *Quarterly Journal of the Royal Meteorological Society, 140*, 687–698.

Cao, S., Wang, Y., Ni, Z., & Xia, B. (2022). Effects of blue-green infrastructures on the microclimate in an urban residential area under hot weather. *Frontiers in Sustainable Cities, 4*, Article 824779.

Carruthers, D. J., & Weng, W. S. (1992). The effect of changes in surface resistance on temperature and humidity fields and fluxes of sensible and latent heat. *Boundary-Layer Meteorology, 60*, 185–199.

Chaston, T. B., Broome, R. A., Cooper, N., Duck, G., Geromboux, C., Guo, Y., Ji, F., Perkins-Kirkpatrick, S., Zhang, Y., & Dissanayake, G. S. (2022). Mortality burden of heatwaves in Sydney, Australia is exacerbated by the urban heat island and climate change: Can tree cover help mitigate the health impacts? *Atmosphere, 13*, 714.

Clinton, N., & Gong, P. (2013). MODIS detected surface urban heat islands and sinks: Global locations and controls. *Remote Sensing of Environment, 134*, 294–304.

Cox, W. & Tikvart, J. 1990. A statistical procedure for determining the best performing air quality simulation model.

Di Sabatino, S., Leo, L. S., Cataldo, R., Ratti, C., & Britter, R. E. (2010). Construction of digital elevation models for a Southern European City and a comparative morphological analysis with respect to Northern European and North American cities. *Journal of Applied Meteorology and Climatology, 49*, 1377–1396.

Digimap. (2024). Available online https://digimap.edina.ac.uk (accessed on 6 June 2024).

Faragallah, R. N., & Ragheb, R. A. (2022). Evaluation of thermal comfort and urban heat island through cool paving materials using ENVI-Met. *Ain Shams Engineering Journal, 13*, Article 101609.

Gao, F., Masek, J., Schwaller, M., & Hall, F. (2006). On the blending of the Landsat and MODIS surface reflectance: Predicting daily Landsat surface reflectance. *IEEE Transactions on Geoscience and Remote sensing, 44*, 2207–2218.

Goodchild, M. F., & Lam, N. S.-N. (1980). Areal interpolation: A variant of the traditional spatial problem. *Geo-processing, 1*, 297–312.

Greenham, S., Jones, S., Ferranti, E., Zhong, J., Acton, J., Mackenzie, A. R., & Grayson, N. (2023). *Mapping climate risk and vulnerability with publicly available data. a guidance document produced by the WM-Air project*. University of Birmingham. https://doi.org/10.25500/epapers.bham.00004259

Haeri, T., Hassan, N., & Ghaffarianhoseini, A. (2023). Evaluation of microclimate mitigation strategies in a heterogenous street canyon in Kuala Lumpur from outdoor thermal comfort perspective using Envi-met. *Urban Climate, 52*, Article 101719.

Hahn, C., Garcia-Marti, I., Sugier, J., Emsley, F., Beaulant, A.-L., Oram, L., Strandberg, E., Lindgren, E., Sunter, M., & Ziska, F. (2022). Observations from personal weather stations—EUMETNET interests and experience. *Climate, 10*, 192.

Hall, J., Zhong, J., Jowett, S., Mazzeo, A., Thomas, G. N., Bryson, J. R., Dewar, S., Inglis, N., Wolstencroft, M., Muller, C., Bloss, W. J., Harrison, R. M., & Bartington, S. E. (2024). Regional impact assessment of air quality improvement: The air quality lifecourse assessment tool (AQ-LAT) for the West Midlands combined authority (WMCA) area. *Environmental Pollution*, Article 123871.

Hamilton, I., Stocker, J., Evans, S., Davies, M., & Carruthers, D. (2014). The impact of the London Olympic Parkland on the urban heat island. *Journal of Building Performance Simulation, 7*, 119–132.

He, J., Liu, J., Zhuang, D., Zhang, W., & Liu, M. (2007). Assessing the effect of land use/land cover change on the change of urban heat island intensity. *Theoretical and Applied Climatology, 90*, 217–226.

Isaya Ndossi, M., & Avdan, U. (2016). Application of open source coding technologies in the production of land surface temperature (LST) maps from Landsat: A PyQGIS plugin. *Remote Sensing, 8*, 413.

Jandaghian, Z., & Berardi, U. (2020). Comparing urban canopy models for microclimate simulations in Weather Research and Forecasting Models. *Sustainable Cities and Society, 55*, Article 102025.

Jänicke, B., Milošević, D., & Manavvi, S. (2021). Review of user-friendly models to improve the urban micro-climate. *Atmosphere, 12*, 1291.

Khalil, M., & Kumar, J. S. (2024). *Time-series studies of land surface temperature in Damascus, Syria through Modis by Google Earth engine*. Advances in Space Research.

Kousis, I., Pigliautile, I., & Pisello, A. L. (2021). Intra-urban microclimate investigation in urban heat island through a novel mobile monitoring system. *Scientific Reports, 11*, 9732.

Lascano, R. J., Goebel, T. S., Gitz Iii, D. C., & Stout, J. E. (2024). Evaluation of a wireless solar powered personal weather station. *Agricultural Sciences, 15*, 36–53.

Lee, S. E., Quinn, A. D., & Rogers, C. D. (2016). Advancing city sustainability via its systems of flows: The urban metabolism of Birmingham and its hinterland. *Sustainability, 8*, 220.

Lei, C., Chen, J., Ibáñez, I., Sciusco, P., Shirkey, G., Lei, M., Reich, P., & Robertson, G. P. (2024). Albedo of crops as a nature-based climate solution to global warming. *Environmental Research Letters, 19*, Article 084032.

Levermore, G., Parkinson, J., Lee, K., Laycock, P., & Lindley, S. (2018). The increasing trend of the urban heat island intensity. *Urban Climate, 24*, 360–368.

Liu, Z., Cheng, K. Y., Sinsel, T., Simon, H., Jim, C. Y., Morakinyo, T. E., He, Y., Yin, S., Ouyang, W., & Shi, Y. (2023). Modeling microclimatic effects of trees and green roofs/façades in ENVI-met: Sensitivity tests and proposed model library. *Building and Environment, 244*, Article 110759.

Lokoshchenko, M. A., & Alekseeva, L. I. (2023). Influence of meteorological parameters on the urban heat island in Moscow. *Atmosphere, 14*, 507.

Luo, X., Vahmani, P., Hong, T., & Jones, A. (2020). City-scale building anthropogenic heating during heat waves. *Atmosphere, 11*, 1206.

Macdonald, R. W., Griffiths, R. F., & Hall, D. J. (1998). An improved method for the estimation of surface roughness of obstacle arrays. *Atmospheric Environment, 32*, 1857–1864.

Maggiotto, G., Buccolieri, R., Santo, M. A., Leo, L. S., & Di Sabatino, S. (2014). Validation of temperature-perturbation and CFD-based modelling for the prediction of the thermal urban environment: The Lecce (IT) case study. *Environmental Modelling & Software, 60*, 69–83.

Mirzaei, M., Verrelst, J., Arbabi, M., Shaklabadi, Z., & Lotfizadeh, M. (2020). Urban heat island monitoring and impacts on citizen's general health status in Isfahan metropolis: A remote sensing and field survey approach. *Remote Sensing, 12*, 1350.

Morton, R. D., Marston, C. G., Neil, A. W., & Rowland, C. S. (2020). *Land cover map 2019 (20m classified pixels, GB)*. NERC Environmental Information Data Centre.

Murie, A., Beazley, M., & Carter, D. (2005). *The birmingham case. metropolitan governance and spatial planning*. Routledge.

Nascimento, C., Demattê, J. A. M., Mello, F., Rosas, J., Tayebi, M., Bellinaso, H., Greschuk, L., Albarracín, H., & Ostovari, Y. (2022). Soil degradation detected by temporal satellite image in São Paulo state. *Brazil. Journal of South American Earth Sciences, 120*, Article 104036.

Naserikia, M., Hart, M. A., Nazarian, N., Bechtel, B., Lipson, M., & Nice, K. A. (2023). Land surface and air temperature dynamics: The role of urban form and seasonality. *Science of The Total Environment, 905*, Article 167306.

Neog, R. (2021). Analyzing dynamic behavior of land use and land surface temperature in the city of Imphal, India. *Acta Geophysica, 69*, 2275–2290.

Oke, T. R. (1987). *Boundary layer climates/T.R. oke*. London: London: Methuen, 2nd ed.

Openstreetmap. (2019). England [Online]. Available Https://download.geofabrik.de/europe/united-kingdom/england.html Accessed 29 March 2024.

Peng, X., Wu, W., Zheng, Y., Sun, J., Hu, T., & Wang, P. (2020). Correlation analysis of land surface temperature and topographic elements in Hangzhou, China. *Scientific Reports, 10*, Article 10451.

Perry, S. G., Cimorelli, A. J., Paine, R. J., Brode, R. W., Weil, J. C., Venkatram, A., Wilson, R. B., Lee, R. F., & Peters, W. D. (2005). AERMOD: A dispersion model for industrial source applications. Part II: Model performance against 17 field study databases. *Journal of Applied Meteorology, 44*, 694–708.

Phelan, P. E., Kaloush, K., Miner, M., Golden, J., Phelan, B., Silva Iii, H., & Taylor, R. A. (2015). Urban heat island: Mechanisms, implications, and possible remedies. *Annual Review of Environment and Resources,, 40*, 285–307.

Piracha, A., & Chaudhary, M. T. (2022). Urban air pollution, urban heat island and human health: A review of the literature. *Sustainability, 14*, 9234.

Qian, J., Meng, Q., Zhang, L., Schlink, U., Hu, X., & Gao, J. (2023). Characteristics of anthropogenic heat with different modeling ideas and its driving effect on urban

heat islands in seven typical Chinese cities. *Science of The Total Environment, 886*, Article 163989.
Raupach, M. R., Weng, W. S., Carruther, D. J., & Huntd, J. C. R. (1992). Temperature and humidity fields and fluxes over low hills. *Quarterly Journal of the Royal Meteorological Society, 118*, 191–225.
Roy, B., Bari, E., Nipa, N. J., & Ani, S. A. (2021). Comparison of temporal changes in urban settlements and land surface temperature in Rangpur and Gazipur Sadar, Bangladesh after the establishment of city corporation. *Remote Sensing Applications: Society and Environment, 23*, Article 100587.
Russell, G. (1980). Crop evaporation, surface resistance and soil water status. *Agricultural Meteorology, 21*, 213–226.
Sajib, M. Q. U., & Wang, T. (2020). Estimation of land surface temperature in an agricultural region of Bangladesh from Landsat 8: Intercomparison of four algorithms. *Sensors, 20*, 1778.
Santamouris, M. (2020). Recent progress on urban overheating and heat island research. Integrated assessment of the energy, environmental, vulnerability and health impact. Synergies with the global climate change. *Energy and Buildings, 207*, Article 109482.
Stull, R. B. (1988). *An introduction to boundary layer meteorology*. Dordrecht London: Kluwer Academic Publishers.
Sun, T., Sun, R., & Chen, L. (2020). The trend inconsistency between land surface temperature and near surface air temperature in assessing urban heat island effects. *Remote Sensing, 12*, 1271.
Theethai Jacob, A., Jayakumar, A., Gupta, K., Mohandas, S., Hendry, M. A., Smith, D. K., Francis, T., Bhati, S., Parde, A. N., & Mohan, M. (2023). Implementation of the urban parameterization scheme in the Delhi model with an improved urban morphology. *Quarterly Journal of the Royal Meteorological Society, 149*, 40–60.
Tiwari, A., Kumar, P., Kalaiarasan, G., & Ottosen, T.-B. (2021). The impacts of existing and hypothetical green infrastructure scenarios on urban heat island formation. *Environmental Pollution, 274*, Article 115898.
Tong, S., Prior, J., Mcgregor, G., Shi, X. & Kinney, P. 2021. Urban heat: An increasing threat to global health. bmj, 375.
Usgs. (2019). *Landsat 8 data users handbook*. Reston: United States Geological Survey.
Virk, G., Jansz, A., Mavrogianni, A., Mylona, A., Stocker, J., & Davies, M. (2015). Microclimatic effects of green and cool roofs in London and their impacts on energy use for a typical office building. *Energy and Buildings, 88*, 214–228.
Vujovic, S., Haddad, B., Karaky, H., Sebaibi, N., & Boutouil, M. (2021). Urban heat island: Causes, consequences, and mitigation measures with emphasis on reflective and permeable pavements. *CivilEng, 2*, 459–484.
Wang, K., Aktas, Y. D., Stocker, J., Carruthers, D., Hunt, J., & Malki-Epshtein, L. (2019). Urban heat island modelling of a tropical city: Case of Kuala Lumpur. *Geoscience Letters, 6*, 1–11.
Xiang, Y., Zheng, B., Bedra, K. B., Ouyang, Q., Liu, J., & Zheng, J. (2023). Spatial and seasonal differences between near surface air temperature and land surface temperature for Urban Heat Island effect assessment. *Urban Climate, 52*, Article 101745.
Xu, M., Deng, F., Jia, S., Jia, X., & Plaza, A. J. (2022). Attention mechanism-based generative adversarial networks for cloud removal in Landsat images. *Remote Sensing Of Environment, 271*, Article 112902.
Zheng, Y., Li, W., Fang, C., Feng, B., Zhong, Q., & Zhang, D. (2023). Investigating the impact of weather conditions on urban heat island development in the subtropical city of Hong Kong. *Atmosphere, 14*, 257.